

Ammonia Production

Asymmetric Manganese Sites in Covalent Organic Frameworks for Efficient Nitrate-to-Ammonia Electrocatalysis

Xuewen Li⁺, Shuai Xia⁺, Shuai Yang, Xiubei Yang, Shuang Zheng, Xiaoyu Xu, Yan Wang,*
Qing Xu,* and Zheng Jiang*

Abstract: The electrocatalytic nitrate reduction reaction (NO₃[−]RR) holds tremendous potential for remediating NO₃[−] pollution while enabling clean ammonia (NH₃) production. However, most catalysts achieve high conversion efficiency relying on high NO₃[−] concentrations. How to catalyze the NO₃[−]RR with a low concentration of NO₃[−] is still a challenge due to the competing hydrogen evolution reaction (HER). Herein, we constructed a novel asymmetric isolated Mn atom based on N-coordination covalent organic framework (COF) (ImPy-COF-Mn), for efficient NO₃[−]RR at a low NO₃[−] concentration of 2 mg mL^{−1}. This bidentate-coordinated COF featured a robust and chemically stable framework, while the synergistic interaction between asymmetric imine N and pyridine N modified the charge distribution of Mn atoms to optimize catalytic efficiency. ImPy-COF-Mn demonstrated remarkable catalytic performance, with 95.64% NH₃ selectivity and a maximum NH₃ yield rate of 1927 mmol h^{−1} g_{cat}^{−1}, exceeding the corresponding parameters of symmetric Mn sites by factors of 1.27 and 1.41, respectively. In situ ATR-FTIR measurements and theoretical calculations revealed that the asymmetric isolated Mn facilitated a reduction in the energy barrier for *NO-to-*NOH conversion, and thus contributed to higher activity and selectivity.

Introduction

Groundwater is a vital freshwater source for human consumption.^[1,2] However, in recent years, human activities have led to a substantial increase in nitrate (NO₃[−]) concentrations in groundwater, surpassing the limits set by the World Health Organization (WHO).^[3,4] This contamination has threatened human health and compromised agricultural product quality, necessitating effective NO₃[−] mitigation strategies.^[5,6] The electrocatalytic NO₃[−] reduction reaction (NO₃[−]RR) has emerged as a promising approach for addressing NO₃[−] pollution while simultaneously gener-

ating clean ammonia (NH₃), a crucial chemical for various industrial applications.^[7–9] Traditionally, industrial NH₃ production has relied on the Haber–Bosch process, which is energy intensive.^[10] As a more energy-efficient alternative, electrochemical NH₃ synthesis via the NO₃[−]RR has gained attention.^[11,12] To date, various NO₃[−]RR electrocatalysts have been developed, including metal nanoparticles,^[13] alloys,^[14] metal oxides,^[15] single-atom catalysts,^[16] and metal–organic frameworks.^[17] However, the practical application of these catalysts remains challenging owing to the high cost and suboptimal energy conversion efficiency of inorganic electrocatalysts, as well as the relatively low stability of MOF-based electrocatalysts. Although most NO₃[−]RR investigations achieve high NH₃ yields at elevated NO₃[−] concentrations (>6192 ppm), developing efficient catalysts for practical low-concentration scenarios (1000–2000 ppm) in industrial wastewater remains challenging due to competing hydrogen evolution reaction (HER) that suppresses yield rates.^[18]

Covalent organic frameworks (COFs),^[19–21] characterized by well-defined structures linked by covalent bonds, have demonstrated notable potential in various electrocatalytic reactions, including the carbon dioxide reduction reaction,^[22,23] H₂O₂ synthesis,^[24] and the oxygen reduction reaction.^[25,26] These frameworks provide a platform for electrocatalytically active sites and a programmable topological architecture that enables precise coordination.^[27–30] Recently, porphyrin (MN₄) planar configurations or bipyridine-based symmetric MN₂X₂ motifs in COFs have been adopted as the catalytic centers for NO₃[−]RR. For example, Hu et al.^[31] fabricated an iron-porphyrin-based COF that achieved a Faradaic efficiency for NH₃(FE_{NH3}) of 85.4% and an NH₃ yield rate


[*] X. Li⁺, Dr. S. Yang, Prof. Z. Jiang
National Synchrotron Radiation Laboratory, University of Science and Technology of China, Hefei 230029, P.R. China
E-mail: jiangz@ustc.edu.cn

X. Li⁺, X. Yang, S. Zheng, X. Xu, Prof. Q. Xu
Advanced Separation & Conversion on Engineered Nanopore Dynamics Laboratory, Shanghai Advanced Research Institute (SARI), Chinese Academy of Sciences (CAS), Shanghai 201210, P.R. China
E-mail: xuqing@sari.ac.cn

X. Li⁺, X. Yang, S. Zheng, X. Xu, Prof. Q. Xu
School of Chemical Engineering, University of Chinese Academy of Sciences, Beijing 100049, P.R. China

S. Xia⁺, Prof. Y. Wang
School of Materials Science and Engineering, Hefei University of Technology, Hefei 230009, P.R. China
E-mail: stone@hfut.edu.cn

[†] Both authors contributed equally to this work.

 Additional supporting information can be found online in the Supporting Information section

of $1883.6 \mu\text{mol h}^{-1} \text{mg}^{-1} \text{COF}$ in $0.5 \text{ M K}_2\text{SO}_4/0.1 \text{ M KNO}_3$ mixed electrolyte. Li et al.^[32] constructed 1D COFs (NiPc-CZDM-COF) using phthalocyanine building blocks, attaining an FE of 86.3% and an NH_3 yield rate of $19.5 \text{ mg cm}^{-2} \text{h}^{-1}$ in the same electrolyte. Zhu et al.^[33] fabricated a Cu-bipyridine COF film (TpBpy-Cu-F) that achieved FE of 92.7% and an NH_3 yield rate of $14.9 \text{ mg h}^{-1} \text{cm}^{-2}$ in $0.5 \text{ M NaNO}_3/0.5 \text{ M Na}_2\text{SO}_4$. These above COFs construction strategies predominantly rely on symmetric coordination architectures, and the high symmetry limits the directionality of electron and proton transport, thereby constraining improvements in catalytic activity in low concentrations of NO_3^- electrolytes.^[34]

To address this drawback, we designed and synthesized an Mn-embedded asymmetric coordination COF (ImPy-COF-Mn) for NO_3^- RR. In this COF, the electronegativity difference between the imine N and pyridine N induces a variation in the charge density gradient, which facilitates the spatial separation of electron and proton transport channels. Imine N serves as an electron channel and accelerates electron transfer, while the electron-rich domain in pyridine N provides target sites for proton migration.^[35] In contrast, BiPy-COF-Mn, which has a uniform coordination structure, lacks such target sites, hindering the directional migration of protons and electrons and leading to sluggish NH_3 formation. As anticipated, ImPy-COF-Mn demonstrated superior performance, achieving an NO_3^- reduction FE of 95.64% and a maximum NH_3 yield rate of $1927 \text{ mmol h}^{-1} \text{g}_{\text{cat}}^{-1}$ at a low NO_3^- concentration of 2 mg mL^{-1} (2000 ppm), outperforming other reported COF- and MOF-based electrocatalysts to date. In situ ATR-FTIR characterization and DFT calculations confirmed that the asymmetric coordination environment effectively regulated the charge distribution of Mn metal atoms. Moreover, the Mn active sites in ImPy-COF-Mn not only enhanced the adsorption strength of key reaction intermediates but also promoted efficient electron transfer, considerably lowering the energy barrier for NO_3^- reduction.

Results and Discussion

BiPy-COF and ImPy-COF were synthesized using a solvothermal method in an *o*-DCB/*n*-BuOH/HAC solvent system at 120°C for 3 days (Schemes S1 and S2). Details of the fabrication conditions are provided in the Supporting Information. Post-functionalization of the COFs was then performed by directly reacting Mn^{2+} with BiPy-COF and ImPy-COF in methanol at 80°C for 12 h, resulting in the formation of BiPy-COF-Mn and ImPy-COF-Mn (Schemes S3 and S4, Figure 1a,b).

BiPy-COF and ImPy-COF were characterized using Fourier transform infrared (FTIR) spectroscopy (Figure S1). In the recorded spectra, peaks appearing at 1621 cm^{-1} corresponded to the $\text{C}=\text{N}$ groups in BiPy-COF and ImPy-COF, confirming the successful synthesis of both COFs.^[36] In addition, other corresponding characterizations were also confirmed the successful synthesis of BiPy-COF and ImPy-COF (Figure S2). The FTIR spectra also indicated that imine bonds in these compounds remained intact after metal incorporation (Figure S3). Additionally, the introduction

of Mn did not disrupt the framework structure, as the characteristic FTIR signals of BiPy-COF and ImPy-COF were retained. Furthermore, the solid-state carbon nuclear magnetic resonance spectroscopy (^{13}C NMR) spectra of BiPy-COF-Mn and ImPy-COF-Mn revealed peaks at 161.0 and 163.4 ppm, attributed to the carbons in the imine bonds of BiPy-COF-Mn and ImPy-COF-Mn, respectively (Figure S4). Other peaks at 139.3 and 125.1 ppm corresponded to the carbons in the aromatic backbones, further confirming that the framework remained intact after metal incorporation.

The crystallinity of the COFs was characterized using powder X-ray diffraction (PXRD). As depicted in Figure 1c, the PXRD pattern of BiPy-COF displayed three primary diffraction peaks at approximately 1.85° , 3.24° , and 3.77° , corresponding to the (100), (110), and (200) facets, respectively. Structural models of BiPy-COF were constructed, and the experimental PXRD results aligned well with the simulated PXRD pattern for the AA stacking mode (purple line), confirming that BiPy-COF adopts an eclipsed stacking arrangement (Figure S5 and Table S1). Similarly, the PXRD pattern of ImPy-COF is presented in Figure 1d, where a sharp diffraction peak appeared at 2.04° along with a broad peak at 3.78° , corresponding to the (100) and (200) facets, respectively. These results are in good agreement with the simulated PXRD pattern, indicating that the crystal structure follows an AA stacking mode (Figure S5 and Table S2). After the incorporation of Mn^{2+} into the COF, the high crystallinity was retained, and no diffraction peaks corresponding to Mn nanoparticles were observed. This suggests that Mn exists in a coordination structure rather than as metallic Mn nanoparticles within the COF matrix.

To evaluate the permanent porosity of BiPy-COF-Mn and ImPy-COF-Mn, nitrogen adsorption-desorption measurements were performed at 77 K . Based on the N_2 adsorption isotherms, the specific surface areas were $253 \text{ m}^2 \text{g}^{-1}$ for BiPy-COF-Mn and $505 \text{ m}^2 \text{g}^{-1}$ for ImPy-COF-Mn (Figure S7). Furthermore, both COFs displayed type I and type IV isotherms, indicating their microporous and mesoporous structures. The pore sizes for BiPy-COF-Mn were 1.4 and 4.2 nm, which aligned well with the pore size distribution predicted by the simulated model (Figure S8a). Similarly, the pore sizes were 1.3 and 3.4 nm for ImPy-COF-Mn (Figure S8b). The pore volumes for BiPy-COF-Mn and ImPy-COF-Mn were 0.22 and $0.53 \text{ cm}^3 \text{g}^{-1}$, respectively.

Scanning electron microscopy (SEM) and high-resolution transmission electron microscopy (HRTEM) were performed to characterize the morphologies of BiPy-COF-Mn and ImPy-COF-Mn. As depicted in Figures S9 and S10, BiPy-COF-Mn and ImPy-COF-Mn comprised small, irregularly sheet-shaped crystals. Further, the structural characteristics of BiPy-COF-Mn and ImPy-COF-Mn were visualized using HRTEM. In Figure 1e,f, the pores are closely packed, indicating the formation of highly ordered crystalline structures. Energy-dispersive X-ray spectroscopy analysis reveals that C, O, N, Mn, and Cl are uniformly distributed over BiPy-COF-Mn and ImPy-COF-Mn (Figures S11 and S12). Moreover, the Mn and Cl contents are nearly identical (Table S3). To precisely locate the atomically dispersed Mn single atoms, atomic-resolution aberration-corrected high-angle annular dark field (HAADF)

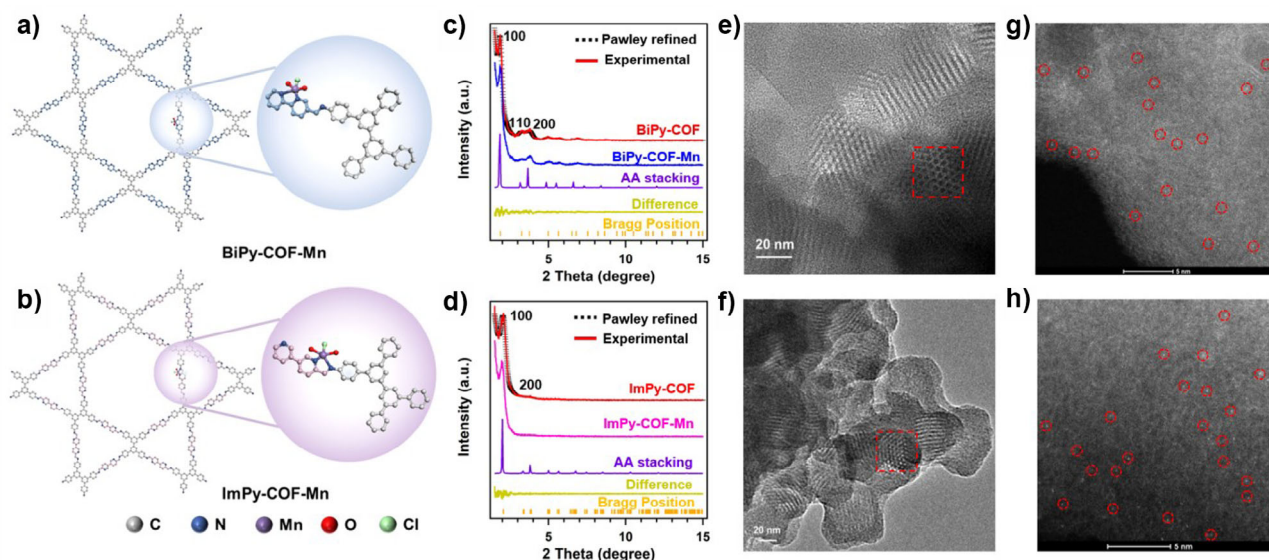


Figure 1. Schematic structures of a) BiPy-COF-Mn and b) ImPy-COF-Mn. PXRD profiles of the experimentally observed (red), Pawley refined (black), different (yellow), Bragg position (orange), and simulated patterns using AA (purple)-stacking modes for c) BiPy-COF and d) ImPy-COF. PXRD profiles of the experimentally observed BiPy-COF-Mn (blue) and ImPy-COF-Mn (pink). HRTEM images of e) BiPy-COF-Mn and f) ImPy-COF-Mn. HAADF-STEM images of g) BiPy-COF-Mn and h) ImPy-COF-Mn.

scanning transmission electron microscopy (STEM) was carried out.^[37,38] Numerous bright spots were identified, marked with red circles in Figure 1g,h, corresponding to Mn atoms. This result was further confirmed by inductively coupled plasma-atomic emission spectroscopy (ICP OES), which revealed that the loading amounts of atomically dispersed Mn were 0.35 wt% and 0.41 wt% in BiPy-COF-Mn and ImPy-COF-Mn, respectively (Table S4). The decomposition temperature for both COFs was above 500 °C under N₂ atmosphere, as determined by thermogravimetric analysis, indicating their high thermal stabilities (Figure S13).

The chemical and structural properties of BiPy-COF-Mn and ImPy-COF-Mn catalysts were examined using X-ray photoelectron spectra (XPS). The full XPS survey scan confirmed the presence of Mn, Cl, C, N, and O in the catalysts (Figure S14 and Table S5).^[39,40] However, given that the Mn and Cl contents were much lower than those of the other elements in the sample, the Mn 2p and Cl 2p peaks were too weak to be clearly observed in the survey scan. The high-resolution Cl 2p XPS spectrum revealed Mn–Cl at binding energies of 197.9 eV, further confirming the presence of Cl in the samples (Figure 2a).^[41,42] The N 1s spectra indicated the presence of C=N, C–N, and Mn–N bonds, confirming the successful introduction of Mn coordinated to bipyridyl groups (Figure 2b). Additionally, the peak position of Mn–N in ImPy-COF-Mn shifted to higher binding energy owing to differences in coordination environments between the two Mn–N motifs. Notably, in BiPy-COF-Mn, both coordinating N atoms originate from the bipyridine group, whereas in ImPy-COF-Mn, one N belongs to the bipyridine group, and the other is part of the imine bond. Furthermore, the Mn 2p XPS spectrum revealed no metallic Mn species in BiPy-COF-Mn and ImPy-COF-Mn, which agreed with the presence of atomically dispersed Mn (Figure S15).^[43,44] Moreover,

the binding energy of Mn species in ImPy-COF-Mn was higher than that in BiPy-COF-Mn, indicating that Mn active sites in BiPy-COF-Mn were more electron-rich than those in ImPy-COF-Mn. The high-resolution O 1s XPS spectrum indicated the presence of abundant O functional groups and the formation of Mn–O bonds in both COFs (Figure 2c). Therefore, the XPS results confirmed the co-coordination of Cl, O, and N with Mn atoms.

The local electronic and atomic structures of the central Mn atom were investigated using X-ray absorption near-edge structure (XANES) and extended X-ray absorption fine structure (EXAFS) analyses. The K-edge XANES curves and the first derivative of the XANES spectra indicated that the absorption edge of ImPy-COF-Mn was closer to that of MnPc than to BiPy-COF-Mn, demonstrating good agreement with the XPS results (Figure 2d and Figure S16).^[45] The phase-uncorrected Fourier-transformed (FT) EXAFS of BiPy-COF-Mn and ImPy-COF-Mn presented a main peak at ~1.73 Å, corresponding to the scattering interaction between Mn atoms and Cl/N/O in the first coordination shell (Figure 2e). The absence of an Mn–Mn bond indicated that Mn clusters or nanoparticles were not present, suggesting that Mn species were atomically dispersed. Unlike the reference MnPc, which exhibited a symmetric peak (Mn–N₄) with an Mn–N scattering path at 1.45 Å in its EXAFS spectrum, BiPy-COF-Mn and ImPy-COF-Mn presented an asymmetric peak with a slight shift. This is attributed to the additional coordination of Mn–Cl in BiPy-COF-Mn and ImPy-COF-Mn and the consequent out-of-plane distortion of Mn atoms.^[46] The coordination configuration of Mn atoms in BiPy-COF-Mn and ImPy-COF-Mn was further investigated through quantitative EXAFS curve fitting analysis (Figures S17 and S18). The best-fitting analysis confirmed that the Mn center was coordinated with one Cl atom and four N/O atoms (Figure 2f

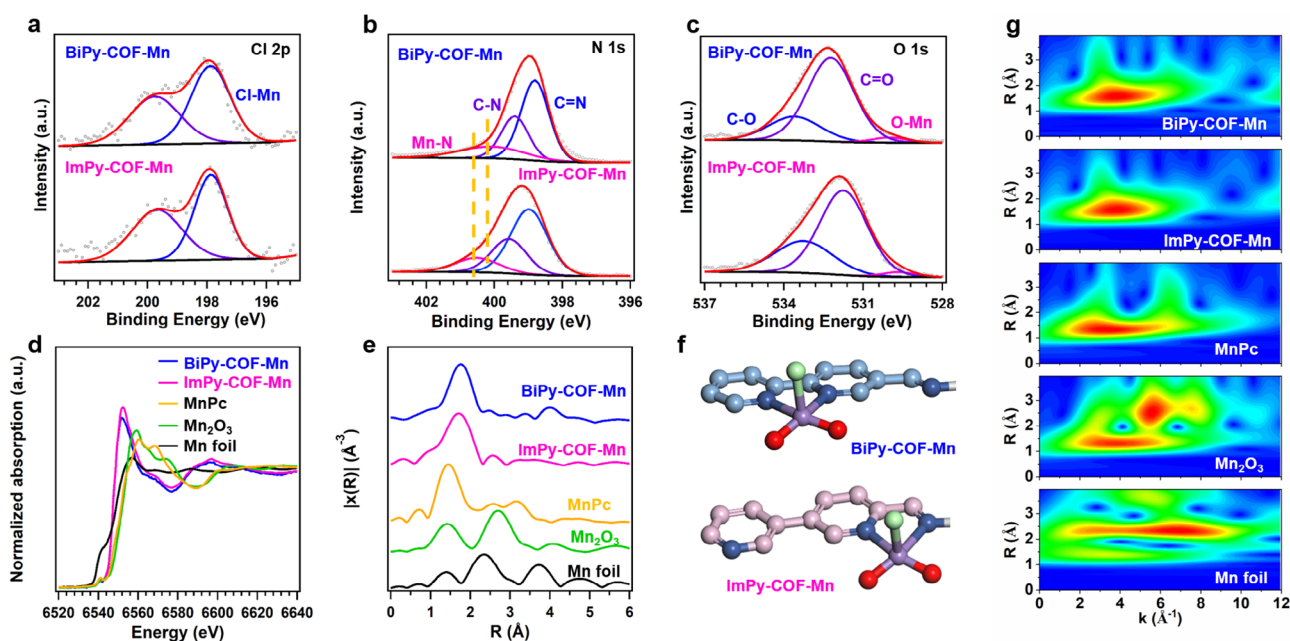


Figure 2. a) Cl 2p XPS spectra, b) N 1s XPS spectra, c) O 1s XPS spectra, d) Mn K-edge XANES spectra, and e) k^3 -weighted FT-EXAFS spectra for BiPy-COF-Mn (blue curve), ImPy-COF-Mn (pink curve), MnPc (orange curve), Mn_2O_3 (green curve), and Mn foil (blue curve). f) Schematic model of BiPy-COF-Mn and ImPy-COF-Mn: Mn (purple), Cl (green), N (blue), and C (azure and pink). g) WT k^2 -weighted Mn K-edge spectra.

and Table S6). In BiPy-COF-Mn, the calculated Mn–N/O bond distance was 2.07 Å, while the Mn–Cl bond distance was 2.60 Å. Meanwhile, in ImPy-COF-Mn, the Mn–N/O bond distance was 2.07 Å, and the Mn–Cl bond distance was 2.58 Å, which was longer than that in MnPc (1.95 Å). Moreover, the wavelet transform (WT) results provided further evidence for the existence of Mn–Cl/N bonding, presenting a maximum at 3.9 Å^{−1} in BiPy-COF-Mn and ImPy-COF-Mn, compared to MnPc, Mn_2O_3 , and Mn foil (Figure 2g).

The electrocatalytic NO_3^- -RR performance of ImPy-COF-Mn and BiPy-COF-Mn electrodes was systematically investigated using an H-cell with a three-electrode system. The products in the electrolyte, including N_2H_4 , NH_3 , and NO_2^- , were quantified using ultraviolet–visible (UV–vis) spectroscopy based on standard calibration curves (Figures S19–S21). Linear sweep voltammetry (LSV) curves of the catalysts were recorded in an electrolyte containing 1 M KOH + NO_3^- (2 mg mL^{−1}) + 0.5 M KF.^[47]

As depicted in Figure 3a, ImPy-COF-Mn exhibited a higher current density than BiPy-COF-Mn, demonstrating its superior NO_3^- -RR activity. To better investigate the catalytic difference between ImPy-COF-Mn and BiPy-COF-Mn, the partial current density curves were also evaluated (Figure S22).^[48] Notably, ImPy-COF-Mn also exhibited a higher NH_3 partial current density than BiPy-COF-Mn. Time-dependent current density curves were recorded for both catalysts, along with the corresponding UV–vis absorption spectra of the electrolyte at various applied potentials after the NO_3^- -RR (Figures S23 and S24). Notably, the ImPy-COF-Mn catalyst delivered higher current densities than BiPy-COF-Mn at equivalent potentials, as reflected in the chronoamperometric curves, indicating faster reaction kinetics for the NO_3^- -RR. To further understand the reaction

process, the catalytic kinetics of the NO_3^- -RR on different catalysts were evaluated using electrochemical impedance spectroscopy (EIS). ImPy-COF-Mn exhibited lower charge transfer resistance than BiPy-COF-Mn, indicating faster charge transfer rates (Figure S25).

Notably, compared to BiPy-COF-Mn, ImPy-COF-Mn demonstrated a higher FE_{NH_3} and NH_3 yield rate at each potential (Figure 3b,c). The highest FE_{NH_3} of ImPy-COF-Mn reached 95.64% at −0.7 V versus RHE, considerably higher than that of BiPy-COF-Mn (75.51%). Moreover, at −0.7 V, ImPy-COF-Mn achieved an NH_3 yield rate of 756 mmol h^{−1} g_{cat}^{−1}. As the cathodic potential increased, the NH_3 yield rate continued to rise within the tested potential range, reaching 1927 mmol h^{−1} g_{cat}^{−1} at −0.9 V, which is higher than that of BiPy-COF-Mn. The decrease in FE_{NH_3} and NH_3 yield rate at higher potentials was attributed to the competitive hydrogen evolution reaction. Furthermore, metal-free ImPy-COF and BiPy-COF have much inferior selectivity of <25%, which clearly manifests the critical role of Mn active centers during the NO_3^- -RR (Figure S26). Moreover, to provide deeper insight into the intrinsic activity of Mn sites, taking the calculation of the turnover frequency (TOF) at −0.9 V as an example, TOF values of ImPy-COF-Mn and BiPy-COF-Mn were 7.2 and 6.1 s^{−1}, respectively, reflecting that the intrinsic activity of ImPy-COF-Mn was significantly higher than that of BiPy-COF-Mn.^[49] To elucidate the intrinsic influencing factors of the catalytic performance, we have measured and calculated the electrochemically active surface area (ECSA) by means of electrochemical double layer capacitance (C_{dl}). (Figure S27). The C_{dl} values of ImPy-COF-Mn and BiPy-COF-Mn were 1.8 and 1.6 mF cm^{−2}, indicating ImPy-COF-Mn has a higher active density in the catalytic process.^[50,51] Additionally, to

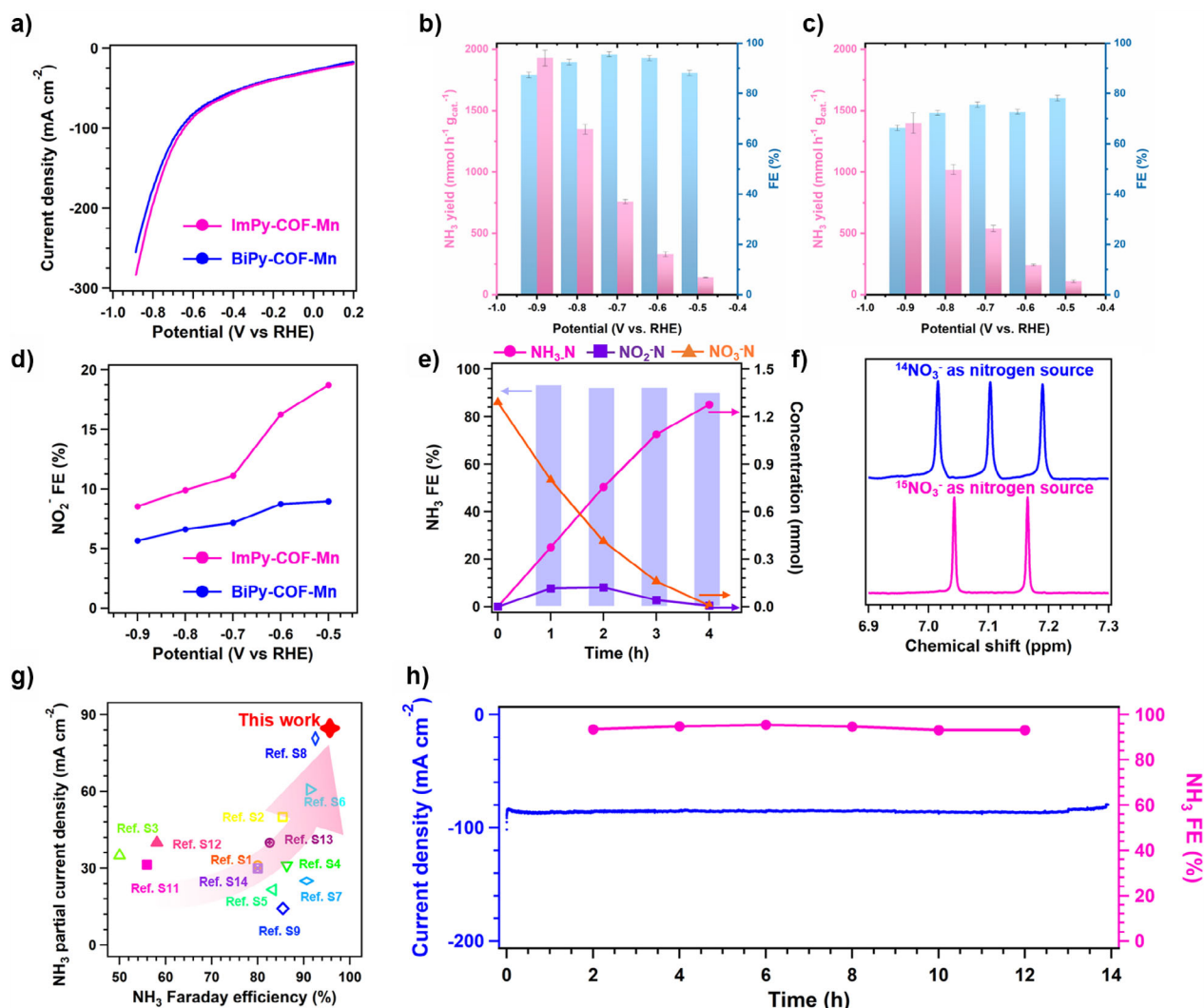


Figure 3. a) LSV curves. NH₃ yield rate and FE of b) ImPy-COF-Mn and c) BiPy-COF-Mn. d) NO₂⁻ FE. e) Ammonia yield as a function of electrolysis time. f) NH₃ produced through the NO₃⁻RR using ¹⁴NO₃⁻ and ¹⁵NO₃⁻ as the N sources. g) Comparison between the NH₃ yield rate and NH₃ FE of ImPy-COF-Mn and the corresponding metrics for reported NO₃⁻RR electrocatalysts. h) Long-term NO₃⁻RR electrolysis and the corresponding FE of NH₃ for ImPy-COF-Mn.

further assess the intrinsic activity of the COFs, the NH₃ partial current density was normalized to the electrochemical surface area. The ECSA-normalized activity maintained the order ImPy-COF-Mn > BiPy-COF-Mn, further demonstrating ImPy-COF-Mn's superior intrinsic activity (Figure S28).

Figure 3d indicates that the FE for NO₂⁻ reduction gradually decreased with increasing negative potential, suggesting that NO₂⁻, as a major intermediate, was reduced to NH₃. As depicted in Figure 3e, the concentration of NO₃⁻ continuously decreased over the reaction duration. Meanwhile, the concentration of NO₂⁻ increased during the first 2 h and then decreased to nearly 0 mmol, while the amount of NH₃ increased to 1.28 mmol after 4 h, which was close to the initial NO₃⁻ amount (1.29 mmol). This result indicates a high conversion efficiency of NO₃⁻ to NH₃. Notably, after electrolysis, the residual NO₃⁻-N was close to the drinking water regulation set by the WHO (<11 µg mL⁻¹).

Additionally, isotope labeling experiments were conducted using aqueous solutions of ¹⁴NO₃⁻ and ¹⁵NO₃⁻ to

identify the products via ¹H NMR. For the NO₃⁻RR at -0.7 V for 1 h, an electrolyte containing 2 mg mL⁻¹ of ¹⁴N-labeled or ¹⁵N-labeled electrolyte was used. The ¹H NMR spectra revealed only two primary peaks for ¹⁵NO₃⁻, distinctly different from the three peaks observed for ¹⁴NO₃⁻ (Figure 3f). These findings confirm that NH₃ originates from the electrocatalytic NO₃⁻RR rather than contamination. Notably, a comparison between the electrocatalytic NO₃⁻RR performance of ImPy-COF-Mn and previously reported COF and MOF catalysts in terms of the NH₃ yield rate and FE_{NH3} highlighted ImPy-COF-Mn's potential for NH₃ synthesis (Figure 3g and Table S8). Additionally, no N₂H₄ was detected in the electrolyte at different applied potentials, as determined by UV-vis spectroscopy (Figure S29). The durability of ImPy-COF-Mn was further evaluated through consecutive electrolysis at -0.7 V. The current density and FE_{NH3} remained stable even at 85.60 mA cm⁻² for over 14 h, demonstrating the excellent stability of the electrocatalytic NO₃⁻RR for NH₃ production. (Figure 3h). Furthermore,

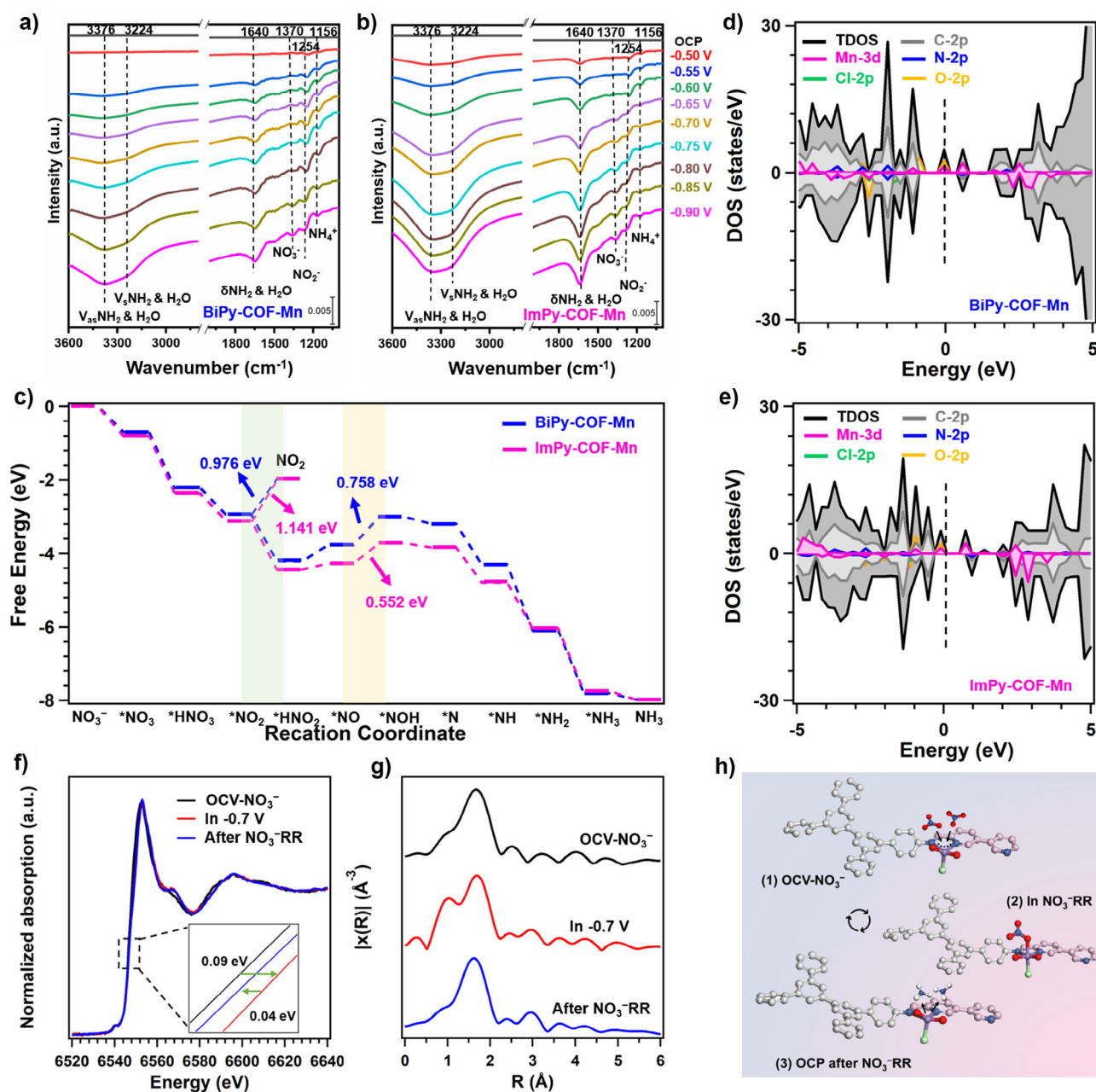


Figure 4. In situ ATR-FTIR spectra of a) BiPy-COF-Mn and b) ImPy-COF-Mn. c) Energetic reaction pathways of the NO_3^- RR to NH_3 on BiPy-COF-Mn (blue) and ImPy-COF-Mn (pink). Projected density of states (PDOS) spectra of d) BiPy-COF-Mn and e) ImPy-COF-Mn. f) Mn K-edge XANES and g) EXAFS spectra of ImPy-COF-Mn under various in situ XAS conditions. h) Activation of molecules at the Mn site.

HAADF-STEM, XRD, and FTIR characterization of the ImPy-COF-Mn after long-term electrolysis revealed that the structure was well retained and Mn sites were atomically dispersed without aggregation, further attesting to its considerable stability (Figures S30–S32). The ICP-OES analysis results revealed that the concentration of Mn in the electrolyte solution was 0.0007 mg L^{-1} , the loss rate was approximately 1.3%, confirming negligible leaching.

To elucidate the mechanism of the NO_3^- RR on ImPy-COF-Mn and BiPy-COF-Mn, In situ attenuated total reflectance (ATR-FTIR) spectroscopy was performed to monitor surface-adsorbed intermediates during the reaction

(Figure 4a,b).^[52] The results suggested that both catalysts follow the same reaction pathway for the NO_3^- RR. No apparent peaks were observed in the FTIR spectra at the open-circuit potential (OCP). Upon applying a potential, a gradually intensifying peak at 1156 cm^{-1} indicated the accumulation of NH_4^+ products, while the intense peaks at 1254 cm^{-1} corresponded to the *NO_2 . Moreover, the vibration peaks at 3376 , 3224 , and 1640 cm^{-1} were attributed to VasNH_2 & H_2O , VsNH_2 & H_2O , and δNH_2 & H_2O , respectively.^[53,54] These characteristic peaks confirm the formation of NH_3 . Additionally, a diminishing peak at 1370 cm^{-1} indicated the continuous consumption of *NO_3^- . Notably, the

ImPy-COF-Mn electrode exhibited higher peak intensity for the NH_2 intermediate compared to the BiPy-COF-Mn electrode at the same applied potential, indicating its stronger adsorption ability for NH_2 intermediate. In situ ATR-FTIR results supported the following pathway for the electrocatalytic NO_3^- -RR to NH_3 : $\text{NO}_3^- \rightarrow ^*\text{NO}_3 \rightarrow ^*\text{NO} \rightarrow ^*\text{N} \rightarrow ^*\text{NH} \rightarrow ^*\text{NH}_2 \rightarrow ^*\text{NH}_3$.^[55,56]

Based on the reaction intermediates identified by in situ ATR-FTIR spectroscopy, density functional theory (DFT) calculations were performed to elucidate the pathways for the NO_3^- -RR on the BiPy-COF-Mn and ImPy-COF-Mn catalysts (Figures S33 and S34). According to our in situ spectroscopy measurements and previous reports, the electrocatalytic reduction of NO_3^- to NH_3 on transition metals involves an eight-electron, nine-proton transfer process.^[57] First, NO_3^- is adsorbed onto the COF surface, followed by its deoxygenation to $^*\text{NO}_2$ and then to $^*\text{NO}$. Subsequently, $^*\text{NO}$ undergoes hydrogenation through the sequence $\rightarrow ^*\text{NOH} \rightarrow ^*\text{N} \rightarrow ^*\text{NH} \rightarrow ^*\text{NH}_2 \rightarrow ^*\text{NH}_3$. Notably, the $^*\text{NO} \rightarrow ^*\text{NOH}$ step was identified as the rate-determining step for both COFs (Figure 4c). ImPy-COF-Mn exhibited a lower endothermic Gibbs free energy change (ΔG) of 0.552 eV compared to BiPy-COF-Mn (0.758 eV), indicating that Mn atoms in ImPy-COF-Mn serve as more active sites for the NO_3^- -RR. Furthermore, the Gibbs free energy barrier for the formation of NO_2 byproducts from $^*\text{NO}_2$ was lower for BiPy-COF-Mn (0.976 eV) than that for ImPy-COF-Mn (1.141 eV), suggesting that BiPy-COF-Mn facilitates byproduct formation. Overall, these findings highlight that ImPy-COF-Mn favors NH_3 generation, demonstrating both thermodynamic feasibility and improved selectivity.^[58]

To further investigate differences in the electronic structures of the two catalysts, the projected density of states (PDOS) analysis was conducted to examine their localized electronic states near the Fermi level (E_F), providing insights into their catalytic activity. The peaks of the Mn 3d, N 2p, O 2p, and Cl 2p orbitals near the Fermi level overlapped considerably, indicating effective electron transfer in the catalysts. As illustrated in Figure 4d,e, the d-band center of ImPy-COF-Mn is located at -0.885 eV, which is closer to the Fermi level compared to the d-band center location of -1.150 eV for BiPy-COF-Mn. This suggests that ImPy-COF-Mn demonstrates better adsorption of reaction intermediates. The enhanced interaction between Mn atoms and the ImPy-COF framework increases charge localization around Mn, promoting the polarization and activation of NO_3^- and facilitating its reduction. Moreover, the electrostatic potential (ESP) distributions and Bader charge of both ImPy-COF-Mn and BiPy-COF-Mn were calculated to verify the different roles of imine-N and pyridine-N (Figure S35). The results revealed that the pyridine-N (1.197 eV) exhibited a more negative charge compared to the imine-N (1.107 eV) in ImPy-COF-Mn. Thus, pyridine-N atoms acted as electron-rich centers (higher negative charge) that facilitated proton migration, while less negative charge imine-N atoms generated a high-speed channel for electron transport.^[59] In addition, the Mn site in ImPy-COF-Mn had the more negative Bader charge than that from BiPy-COF-Mn, which contributed to easier absorbing NO_3^- .^[60]

To elucidate the structures and chemical states of the active sites in ImPy-COF-Mn during the NO_3^- -RR, in situ X-ray absorption spectroscopy (XAS) measurements were conducted under various catalytic conditions.^[61] XANES spectra recorded under these conditions revealed that the Mn K-edge of as-prepared ImPy-COF-Mn shifted to higher energy under the reaction conditions at -0.7 V versus RHE compared to the conditions at the OCP. This shift can be attributed to an increase in the Mn oxidation state due to electron redistribution following NO_3^- adsorption at the Mn site. Specifically, electrons transferred from the Mn site to the N 2p orbital, forming an $\text{NO}_3^{\delta-}$ species (Figure 4f). When a potential of -0.7 V was applied to the electrode, electrocatalytic NO_3^- reduction occurred, and subsequently, the Mn K-edge shifted back to a lower energy, indicating that the Mn valence state returned to a relatively low oxidation state after one cycle of NO_3^- reduction. This behavior suggests ongoing NO_3^- reduction and remarkable NO_3^- activation ability of the Mn center. Interestingly, the minor variations in oxidation state changes highlight the crucial influence of Cl coordination on Mn oxidation states during the NO_3^- -RR. Meanwhile, in the FT-EXAFS spectra, bond length exhibited minimal changes throughout the reaction (Figure 4g). Best-fitting analyses revealed that the Mn–N/O coordination number increased at -0.7 V relative to the OCP, both before and after the reaction. This increase can be attributed to the formation of an additional Mn–O bond due to the interaction of NO_3^- with the Mn center (Figures S36–S38 and Table S7). Additionally, the Mn–N/O bond length shortened to 2.00 Å, while the Mn–Cl bond length increased during the NO_3^- -RR at -0.7 V. This observation suggests that Mn atoms, initially distorted out of the COF plane at the OCP, underwent structural reconfiguration upon NO_3^- reduction, with Mn being slightly pulled back into the plane due to Mn–N bond formation (Figure 4h). The in situ XAS results indicate that the $\text{MnN}_2\text{O}_2\text{Cl}$ site in ImPy-COF-Mn serves as the active site for the NO_3^- -RR, where NO_3^- is adsorbed, activated, and converted.^[62]

Conclusion

In summary, we fabricated and examined two Mn-centered COFs, BiPy-COF-Mn (symmetric bipyridine N-coordination) and ImPy-COF-Mn (asymmetric pyridine-imine N-coordination), to elucidate the atomic-level influence of Mn on the NO_3^- -RR. The results revealed that the imine N in ImPy-COF-Mn exhibited stronger electron-withdrawing capability, enhancing electron transfer to the Mn center. Meanwhile, the electron-rich domain in pyridine N facilitated H migration. This electronic modulation endowed ImPy-COF-Mn with superior electrocatalytic performance, achieving a higher FE (95.64%), and NH_3 yield ($1927 \text{ mmol h}^{-1} \text{ g}_{\text{cat}}^{-1}$) than BiPy-COF-Mn, particularly at low NO_3^- concentrations. In situ ATR-FTIR spectroscopy, theoretical calculations, and in situ XAS analyses revealed that the dual N-coordination created synergistic adsorption–activation sites, promoting the formation of the key intermediate $^*\text{NOH}$ on ImPy-COF-Mn. Overall, this study proposes an asymmetric coordination strategy

for designing targeted electrocatalysts for nitrogen cycle applications.

Supporting Information

The detailed experimental section, additional figures, and tables are listed in the Supporting Information file. The authors have cited additional references within the Supporting Information.

Acknowledgements

The authors acknowledge the financial supports from the National Key Research and Development Program (2022YFA1503801), the National Natural Science Foundation of China (52272289 and 52172293), the Youth Innovation Promotion Association of Chinese Academy of Sciences (E324441401). The authors would also thank beamline BL01B of the National Synchrotron Radiation Laboratory (NSRL, China) for the beam time allocation and assistance. The authors would also thank beamline BL20U1 and BL14W1 at SSRF for the beam time allocation and assistance. The authors would like to thank Suzhou Deyo Bot Advanced Materials Co., Ltd. (www.dy-test.com) for providing support on material characterization.

Conflict of Interests

The authors declare no conflict of interest.

Data Availability Statement

Research data are not shared.

Keywords: Asymmetric coordination • Covalent organic framework • Electrocatalysis • Manganese-based COF • Nitrate reduction reaction

- [1] H. Xu, Y. Ma, J. Chen, W.-x. Zhang, J. Yang, *Chem. Soc. Rev.* **2022**, *51*, 2710–2758.
- [2] F.-Y. Chen, A. Elgazzar, S. Pecaut, C. Qiu, Y. Feng, S. Ashokkumar, Z. Yu, C. Sellers, S. Hao, P. Zhu, H. Wang, *Nat. Catal.* **2024**, *7*, 1032–1043.
- [3] Y. Wang, C. Wang, M. Li, Y. Yu, B. Zhang, *Chem. Soc. Rev.* **2021**, *50*, 6720–6733.
- [4] Y. Fan, X. Wang, C. Butler, A. Kankam, A. Belgada, J. Simon, Y. Gao, E. Chen, L. R. Winter, *Nat. Water* **2024**, *2*, 684–696.
- [5] A. Yoon, L. Bai, F. Yang, F. Franco, C. Zhan, M. Rüscher, J. Timoshenko, C. Pratsch, S. Werner, H. S. Jeon, M. C. d. O. Monteiro, S. W. Chee, B. R. Cuenya, *Nat. Mater.* **24**, 762–769.
- [6] J. Guo, M. J. Liu, C. Laguna, D. M. Miller, K. S. Williams, B. D. Clark, C. Muñoz, S. J. Blair, A. C. Nielander, T. F. Jaramillo, W. A. Tarpeh, *Energy Environ. Sci.* **2024**, *17*, 8787–8800.
- [7] Y. Yao, K. Wei, S. Zhao, H. Zhou, B. Kui, G. Zhu, W. Wang, P. Gao, W. Ye, *Chem. Eng.* **2025**, *13*, 1245–1252.
- [8] J. Sun, S. Garg, J. Xie, C. Zhang, T. D. Waite, *Environ. Sci. Technol.* **2022**, *56*, 17298–17309.
- [9] J. Zhang, T. Quast, B. Eid, Y.-T. Chen, R. Zerdoumi, S. Dieckhöfer, J. R. C. Junqueira, S. Seisel, W. Schuhmann, *Nat. Commun.* **2024**, *15*, 8583.
- [10] F.-Y. Chen, Z.-Y. Wu, S. Gupta, D. J. Rivera, S. V. Lambeets, S. Pecaut, J. Y. T. Kim, P. Zhu, Y. Z. Finck, D. M. Meira, G. King, G. Gao, W. Xu, D. A. Cullen, H. Zhou, Y. Han, D. E. Perea, C. L. Muhich, H. Wang, *Nat. Nanotechnol.* **2022**, *17*, 759–767.
- [11] M. J. Liu, J. Guo, A. S. Hoffman, J. H. Stenlid, M. T. Tang, E. R. Corson, K. H. Stone, F. Abild-Pedersen, S. R. Bare, W. A. Tarpeh, *J. Am. Chem. Soc.* **2022**, *144*, 5739–5744.
- [12] W. Jang, D. Oh, J. Lee, J. Kim, J. E. Matthews, H. Kim, S.-W. Lee, S. Lee, Y. Xu, J. M. Yu, S. W. Hwang, T. F. Jaramillo, J.-W. Jang, S. Cho, *J. Am. Chem. Soc.* **2024**, *146*, 27417–27428.
- [13] N. Zhang, J. Shang, X. Deng, L. Cai, R. Long, Y. Xiong, Y. Chai, *ACS Nano* **2022**, *16*, 4795–4804.
- [14] Q. Gao, B. Yao, H. S. Pillai, W. Zhang, X. Han, Y. Liu, S.-W. Yu, Z. Yan, B. Min, S. Zhang, H. Zhou, L. Ma, H. Xin, Q. He, H. Zhu, *Nat. Synth.* **2023**, *2*, 624–634.
- [15] Y. Liu, J. Wei, Z. Yang, L. Zheng, J. Zhao, Z. Song, Y. Zhou, J. Cheng, J. Meng, Z. Geng, J. Zeng, *Nat. Commun.* **2024**, *15*, 3619.
- [16] S. Tang, M. Xie, S. Yu, X. Zhan, R. Wei, M. Wang, W. Guan, B. Zhang, Y. Wang, H. Zhou, G. Zheng, Y. Liu, J. H. Warner, G. Yu, *Nat. Commun.* **2024**, *15*, 6932.
- [17] Z. Wang, S. Liu, M. Wang, L. Zhang, Y. Jiang, T. Qian, J. Xiong, C. Yang, C. Yan, *ACS Catal.* **2023**, *13*, 9125–9135.
- [18] Q. Li, L. Luo, X. Guo, R. Wang, J. Liu, W. Fan, Z. Feng, F. Zhang, *J. Am. Chem. Soc.* **2025**, *147*, 1884–1892.
- [19] S. Kandambeth, K. Dey, R. Banerjee, *J. Am. Chem. Soc.* **2019**, *141*, 1807–1822.
- [20] X. Yang, Q. Xu, W. Wei, G. Zeng, *Angew. Chem. Int. Ed.* **2025**, e202504355, <https://doi.org/10.1002/anie.202504355>.
- [21] A. P. Côté, A. I. Benin, N. W. Ockwig, M. O’Keeffe, A. J. Matzger, O. M. Yaghi, *Science* **2005**, *310*, 1166–1170.
- [22] S. Lin, C. S. Diercks, Y.-B. Zhang, N. Kornienko, E. M. Nichols, Y. Zhao, A. R. Paris, D. Kim, P. Yang, O. M. Yaghi, C. J. Chang, *Science* **2015**, *349*, 1208–1213.
- [23] H. Guo, D.-H. Si, H.-J. Zhu, Z.-A. Chen, R. Cao, Y.-B. Huang, *Angew. Chem. Int. Ed.* **2024**, *63*, e202319472.
- [24] S. An, X. Li, S. Shang, T. Xu, S. Yang, C.-X. Cui, C. Peng, H. Liu, Q. Xu, Z. Jiang, J. Hu, *Angew. Chem. Int. Ed.* **2023**, *62*, e202218742.
- [25] S. Yang, Z. He, X. Li, B. Mei, Y. Huang, Q. Xu, Z. Jiang, *Angew. Chem. Int. Ed.* **2024**, *64*, e202418347.
- [26] H. Chen, D. Li, M. Lin, Q. Wang, Y. Zou, J. Ran, Y. Xing, X. Long, *Adv. Mater.* **2025**, *37*, 2500063.
- [27] X. Zhao, P. Pachfule, A. Thomas, *Chem. Soc. Rev.* **2021**, *50*, 6871–6913.
- [28] P. Hosseini, A. Rodríguez-Camargo, Y. Jiang, S. Zhang, C. Scheu, L. Yao, B. V. Lotsch, K. Tschulik, *Adv. Sci.* **2025**, *12*, 2413555.
- [29] J. Yang, H. Xu, J. Li, K. Gong, F. Yue, X. Han, K. Wu, P. Shao, Q. Fu, Y. Zhu, W. Xu, X. Huang, J. Xie, F. Wang, W. Yang, T. Zhang, Z. Xu, X. Feng, B. Wang, T. Zhang, Z. Xu, X. Feng, B. Wang, *Science* **2024**, *385*, 1115–1120.
- [30] W.-D. Zhang, L. Zhou, Y.-X. Shi, Y. Liu, H. Xu, X. Yan, Y. Zhao, Y. Jiang, J. Zhang, Z.-G. Gu, *Angew. Chem. Int. Ed.* **2023**, *62*, e202304412.
- [31] H. Hu, R. Miao, F. Yang, F. Duan, H. Zhu, Y. Hu, M. Du, S. Lu, *Adv. Energy Mater.* **2024**, *14*, 2302608.
- [32] M. Li, B. Han, L. Gong, Y. Jin, M. Wang, X. Ding, D. Qi, J. Jiang, *Chin. Chem. Lett.* **2024**, 110590.
- [33] Y. Zhu, H. Duan, C. G. Gruber, W. Qu, H. Zhang, Z. Wang, J. Zhong, X. Zhang, L. Han, D. Cheng, D. D. Medina, E. Cortés, D. Zhang, *Angew. Chem. Int. Ed.* **2025**, *64*, e202421821.
- [34] Z. Li, B. Cai, Y. Zou, D. Zhang, Y. Liang, Y. Zhou, Y. Ma, X. Wang, B. Shi, W.-K. Chen, Y. Liu, X. Zhao, *Adv. Energy Mater.* **2025**, 2500341, <https://doi.org/10.1002/anie.202500341>.

- [35] X. Wang, N. Zhang, H. Shang, H. Duan, Z. Sun, L. Zhang, Y. Lei, X. Luo, L. Zhang, B. Zhang, W. Chen, *Nat. Commun.* **2025**, *16*, 470.
- [36] Q. Pan, M. Abdellah, Y. Cao, W. Lin, Y. Liu, J. Meng, Q. Zhou, Q. Zhao, X. Yan, Z. Li, H. Cui, H. Cao, W. Fang, D. A. Tanner, M. Abdel-Hafiez, Y. Zhou, T. Pullerits, S. E. Canton, H. Xu, K. Zheng, *Nat. Commun.* **2022**, *13*, 845.
- [37] P. Fu, C. Chen, C. Wu, B. Meng, Q. Yue, T. Chen, W. Yin, X. Chi, X. Yu, R. Li, Y. Wang, Y. Zhang, W. Luo, X. Liu, Y. Han, J. Wang, S. Xi, Y. Zhou, *Angew. Chem. Int. Ed.* **2025**, *64*, e202415202.
- [38] Y. Zhang, H. Li, X. He, A. Wang, G. Bai, X. Lan, *Green Chem.* **2023**, *25*, 5557–5565.
- [39] H. Zhang, Z. Lin, P. Kidkhunthod, J. Guo, *Angew. Chem. Int. Ed.* **2023**, *62*, e202217527.
- [40] Y. Zeng, X. Tan, Z. Zhuang, C. Chen, Q. Peng, *Angew. Chem. Int. Ed.* **2025**, *64*, e202416715.
- [41] Y. Guo, R. Zhang, S. Zhang, H. Hong, Y. Zhao, Z. Huang, C. Han, H. Li, C. Zhi, *Energy Environ. Sci.* **2022**, *15*, 4167–4174.
- [42] B. Zhang, J. Zhang, J. Shi, D. Tan, L. Liu, F. Zhang, C. Lu, Z. Su, X. Tan, X. Cheng, B. Han, L. Zheng, J. Zhang, *Nat. Commun.* **2019**, *10*, 2980.
- [43] R. Zeng, H. Li, Z. Shi, L. Xu, J. Meng, W. Xu, H. Wang, Q. Li, C. J. Pollock, T. Lian, M. Mavrikakis, D. A. Muller, H. D. Abruña, *Nat. Mater.* **2024**, *23*, 1695–1703.
- [44] Y. Yan, N. Fu, W. Shao, T. Wang, Y. Liu, Y. Niu, Y. Zhang, M. Peng, Z. Yang, *Small* **2024**, *20*, 2311799.
- [45] X. Tong, P. Zhang, P. Chen, Z. He, X. Kang, Y. Yin, Y. Cheng, M. Zhou, L. Jing, C. Wang, B. Xu, L. Zheng, X. Xing, Z. Wu, B. Han, *Angew. Chem. Int. Ed.* **2025**, *64*, e202413005.
- [46] Q. Wang, Y. Tan, S. Tang, W. Liu, Y. Zhang, X. Xiong, Y. Lei, *ACS Nano* **2023**, *17*, 9565–9574.
- [47] Y. Wang, S. Xia, R. Cai, J. Zhang, J. Wang, C. Yu, J. Cui, Y. Zhang, J. Wu, S. Yang, H. H. Tan, Y. Wu, *Small* **2023**, *19*, 2302295.
- [48] W. Yang, H. Liu, X. Chang, Y. Zhang, Y. Cai, Y. Li, Y. Cui, B. Xu, L. Yu, X. Cui, D. Deng, *Nat. Commun.* **2025**, *16*, 1257.
- [49] X. Deng, Y. Yang, L. Wang, X.-Z. Fu, J.-L. Luo, *Adv. Sci.* **2021**, *8*, 2004523.
- [50] H. Liu, J. Timoshenko, L. Bai, Q. Li, M. Rüschler, C. Sun, B. Roldan Cuenya, J. Luo, *ACS Catal.* **2023**, *13*, 1513–1521.
- [51] N.-Y. Huang, B. Chu, D. Chen, B. Shao, Y.-T. Zheng, L. Li, X. Xiao, Q. Xu, *J. Am. Chem. Soc.* **2025**, *147*, 8832–8840.
- [52] Y. Wang, S. Xia, J. Zhang, A. K. Ummireddi, Z. Li, X. Yuan, C. Yu, Y. Zhang, J. Wu, Y. Wu, *Mater. Chem. Front.* **2023**, *7*, 3093–3101.
- [53] W. Ye, Y. Zhang, L. Chen, F. Wu, Y. Yao, W. Wang, G. Zhu, G. Jia, Z. Bai, S. Dou, P. Gao, N. Wang, G. Wang, *Angew. Chem. Int. Ed.* **2024**, *63*, e202410105.
- [54] P. Li, Y. Jiao, Y. Ruan, H. Fei, Y. Men, C. Guo, Y. Wu, S. Chen, *Nat. Commun.* **2023**, *14*, 6936.
- [55] Y. Wang, S. Xia, J. Zhang, Z. Li, R. Cai, C. Yu, Y. Zhang, J. Wu, Y. Wu, *ACS Energy Lett.* **2023**, *8*, 3373–3380.
- [56] Y. Wang, S. Xia, R. Cai, J. Zhang, C. Yu, J. Cui, Y. Zhang, J. Wu, Y. Wu, *Angew. Chem. Int. Ed.* **2024**, *63*, e202318589.
- [57] T. Hu, C. Wang, M. Wang, C. M. Li, C. Guo, *ACS Catal.* **2021**, *11*, 14417–14427.
- [58] J. Yu, Y. Wang, Y. Li, *Phys. Chem. Chem. Phys.* **2024**, *26*, 15120–15124.
- [59] Y. Wang, Y.-H. Zhong, Y.-D. Wang, Y. Ma, X.-Y. Gao, L.-L. Xu, J. He, K.-F. Yung, X.-B. Li, L.-Z. Wu, W.-Y. Wong, *CCS Chem.* **2024**, 1–13, <https://doi.org/10.31635/ccschem.024.202404867>.
- [60] M. Xu, F. Wu, Y. Zhang, Y. Yao, G. Zhu, X. Li, L. Chen, G. Jia, X. Wu, Y. Huang, P. Gao, W. Ye, *Nat. Commun.* **2023**, *14*, 6994.
- [61] H. B. Yang, S.-F. Hung, S. Liu, K. Yuan, S. Miao, L. Zhang, X. Huang, H.-Y. Wang, W. Cai, R. Chen, J. Gao, X. Yang, W. Chen, Y. Huang, H. M. Chen, C. M. Li, T. Zhang, B. Liu, *Nat. Energy* **2018**, *3*, 140–147.
- [62] B. Mei, J. Mao, Z. Liang, F. Sun, S. Yang, J. Li, J. Ma, F. Song, Z. Jiang, F. Song, Z. Jiang, *J. Am. Chem. Soc.* **2025**, *147*, 5819–5827.

Manuscript received: April 02, 2025

Revised manuscript received: April 29, 2025

Accepted manuscript online: May 12, 2025

Version of record online: ■ ■ ■

Research Article

Ammonia Production

X. Li, S. Xia, S. Yang, X. Yang,
S. Zheng, X. Xu, Y. Wang*, Q. Xu*,
Z. Jiang* **e202507479**

Asymmetric Manganese Sites in Covalent
Organic Frameworks for Efficient
Nitrate-to-Ammonia Electrocatalysis

The covalent organic framework with asymmetric imine N and pyridine N coordination alters the charge distribution of manganese atoms and accelerates the electron/proton-oriented transfer, thus improving the catalytic efficiency for the nitrate reduction reaction.

